



# Ni<sub>0.9</sub>Mn<sub>0.1</sub>Fe<sub>2</sub>O<sub>4</sub> nanoparticles preparation and sunlight-utilized photocatalytic activity

O. Raina<sup>1</sup> · B. Prakash<sup>2</sup>

Received: 9 July 2019 / Accepted: 26 October 2019 / Published online: 2 November 2019  
© Springer Nature B.V. 2019

## Abstract

The metal hydrazine precursor of Ni<sub>0.9</sub>Mn<sub>0.1</sub>Fe<sub>2</sub>O<sub>4</sub> nanoparticles was prepared through co-precipitation technique. Infrared spectrum of the precursor was showed the bridging bidentate nature of hydrazine. Multistep endothermic mass loss was observed from the thermogravimetric–differential thermogravimetric curves of the precursor. Ni<sub>0.9</sub>Mn<sub>0.1</sub>Fe<sub>2</sub>O<sub>4</sub> nanoparticles synthesized from the precursor using thermal decomposition technique were characterized by infrared spectroscopy, energy-dispersive spectroscopy, powder X-ray diffraction, scanning electron microscopy, transmission electron microscopy, vibrating sample magnetometry and UV-diffuse reflectance spectroscopy which proposed the phase structure, morphology, magnetic and optical properties. An effective photocatalytic activity has shown by Ni<sub>0.9</sub>Mn<sub>0.1</sub>Fe<sub>2</sub>O<sub>4</sub> nanoparticles on Congo red, malachite green, methylene blue, methyl red, rhodamine B and rose bengal under direct sunlight at different time intervals. The nanoparticles were magnetically separated and showed good recycling ability.

**Keywords** Hydrazine · Ni<sub>0.9</sub>Mn<sub>0.1</sub>Fe<sub>2</sub>O<sub>4</sub> · Photocatalytic activity · Methylene blue · Recycling

## Introduction

Nowadays, increasing demand for freshwater has been seen in many countries including India. Water pollution is one of the major reasons for the water scarcity [1, 2]. Moreover, water contaminations due to dyes from industries [3, 4] worsen the present situation. To overcome these problems, scientists all over the globe have

---

✉ O. Raina  
raina2oliver@gmail.com

<sup>1</sup> Department of Chemistry, Sri Ramakrishna Engineering College, Coimbatore, Tamilnadu 641 022, India

<sup>2</sup> PG and Research Department of Chemistry, Kongunadu Arts and Science College, Coimbatore, Tamilnadu 641 029, India

been cultivating loads of techniques [5–7] day by day. Compared to all techniques, photocatalysis with transition metal oxides [8] and ferrites [9–11] is a cost-effective and an efficient one. Using nickel manganese ferrite as a catalyst, the photocatalytic activity on various dyes was reported earlier [12, 13].

Ferrites are gaining interest due to their versatile magnetic, electrical and optical properties. Because of various applications, mixed transition metal ferrites are also fascinating researchers. In continuation, nickel manganese ferrites prepared by wet chemical with calcinations method [14], reverse micelle technique [15], auto-combustion technique [16], solvothermal technique [17], co-precipitation [18, 19], spray technique [20], evaporation technique [21], mechanical milling [22], sol–gel method [23] are gaining attention and found applications in gas sensors [21] and lithium-ion batteries [19].

Being a unique ligand, hydrazine coordinates with variety of acids and metals to build complexes [24]. Hydrazine derivatives are used as precursors to explore wide range of metal oxides [25, 26] especially mixed metal ferrites [27, 28] for the few decades. However, nickel manganese ferrites from hydrazine derivatives are not yet reported. In this article, preparation and characterization of  $\text{Ni}_{0.9}\text{Mn}_{0.1}\text{Fe}_2\text{O}_4$  nanoparticles from its hydrazine precursor  $\text{Ni}_{0.9}\text{Mn}_{0.1}\text{Fe}_2(\text{C}_8\text{H}_5\text{Cl}_2\text{O}_3)\cdot\text{N}_2\text{H}_4$  are elaborated. Further, an effective photocatalytic activity of the nanoparticles on Congo red (CR), methylene blue (MB), malachite green (MG), methyl red (MR), rhodamine B (RhB) and rose bengal (RB) under sunlight and magnetic separation of the photocatalyst was examined.

## Experimental

### Materials

All of the chemical reagents were purchased from Merck, India, in AR grade and used without further purification. Distilled water was used for all of the solutions. The following reagents were used: 2,4-dichlorophenoxyacetic acid, hydrazine hydrate (99%), iron sulfate heptahydrate, nickel nitrate hexahydrate, manganese acetate heptahydrate, ethanol, diethyl ether, con. hydrochloric acid, carbontetrachloride, CR, MG, MB, MR, RhB, and RB.

### Preparation of $\text{Ni}_{0.9}\text{Mn}_{0.1}\text{Fe}_2\text{O}_4$ nanoparticles

The precursor  $\text{Ni}_{0.9}\text{Mn}_{0.1}\text{Fe}_2(\text{C}_8\text{H}_5\text{Cl}_2\text{O}_3)\cdot\text{N}_2\text{H}_4$  was synthesized via the co-precipitation technique. An aqueous solution (50 ml) of hydrazine hydrate (0.01 mol) and 2,4-dichlorophenoxy acetic acid (0.01 mol) was kept on a water bath for 10 min at 50 °C to get a clear solution. This clear solution added by drops to an aqueous solution (50 ml) containing ferrous sulfate heptahydrate (0.01 mol), nickel nitrate hexahydrate (0.0003 mol) and manganese acetate heptahydrate (0.004 mol). The mixed solution was kept under magnetic stirring for half an hour. The formed yellow precipitate was filtered off, washed with water and alcohol followed by diethyl

ether and air-dried. The dried precursor was thermally decomposed in air for an hour which led to the formation of Ni<sub>0.9</sub>Mn<sub>0.1</sub>Fe<sub>2</sub>O<sub>4</sub> nanoparticles. The as-prepared nanoparticles cooled in a desiccator ground well to powder and preserve in an airtight container.

## Characterization

Infrared (IR) spectra were recorded by the KBr disk technique using a Shimadzu Spectrophotometer. Simultaneous thermogravimetry–differential thermogravimetry (TG–DTA) was carried out in air using Universal V4.5A instrument. Scanning electron microscopy (SEM) and energy-dispersive spectroscopy (EDS) images were performed on a HITACHI Model S-3000H. XRD pattern was recorded using X-ray diffractometer (X'per PRO model) using Cu-K $\alpha$  radiation, at 40 keV in the 2  $\theta$  range of 20°–90°. Transmission electron microscopy (TEM) micrographs were collected on Joel/JEM 2100 instrument. The UV–diffuse reflectance spectrum (UV–DRS) was operated on Shimadzu UV–DRS spectrophotometer. The room-temperature magnetic parameters measurement was performed on Lakeshore VSM 7410. The adsorption and photocatalytic activity studies were carried out on a Shimadzu UV-2550 UV–Vis spectrophotometer.

## Photocatalytic test

The photocatalytic activity of Ni<sub>0.9</sub>Mn<sub>0.1</sub>Fe<sub>2</sub>O<sub>4</sub> nanoparticles was evaluated by the degradation of CR, MG, MB, MR, RhB and RB under bright sunlight. The Ni<sub>0.9</sub>Mn<sub>0.1</sub>Fe<sub>2</sub>O<sub>4</sub> nanoparticles as a catalyst (200 mg) were added into the flask containing 100 mL of dye solutions with an initial concentration of 500 mg L<sup>-1</sup> (initial pH < 6) under magnetic stirring for an hour in the dark to attain adsorption–desorption equilibrium. After that, the suspensions were kept under sunlight and the samples were collected at different time intervals (0, 10, 20, 30, 40, 50 and 60, respectively). The concentrations of dyes were determined by a Shimadzu UV-2550 UV–Vis spectrophotometer at the wavelengths of 496, 664, 615, 532, 550 and 554 nm for CR, MB, MG, MR, RB and RhB, respectively.

## Results and discussion

### Characterization of the precursor

The percentage of hydrazine (7.59%) in the precursor was determined by the titration using KIO<sub>3</sub> as a titrant, by volumetric analysis under Andrew's condition [29]. The image of EDS (Fig. 1a) clearly shows that the precursor comprises with C, N, O, Cl, Ni, Mn and Fe and no other impurities. The elements N and C, O and Cl confirmed that the precursor consists of hydrazine and carboxylate group (C<sub>8</sub>H<sub>5</sub>Cl<sub>2</sub>O<sub>3</sub>), respectively. In the FTIR spectrum of the precursor (Fig. 1b), the sharp peak at 3294 cm<sup>-1</sup> attributed to the N–H stretching frequency. The separation of asymmetric

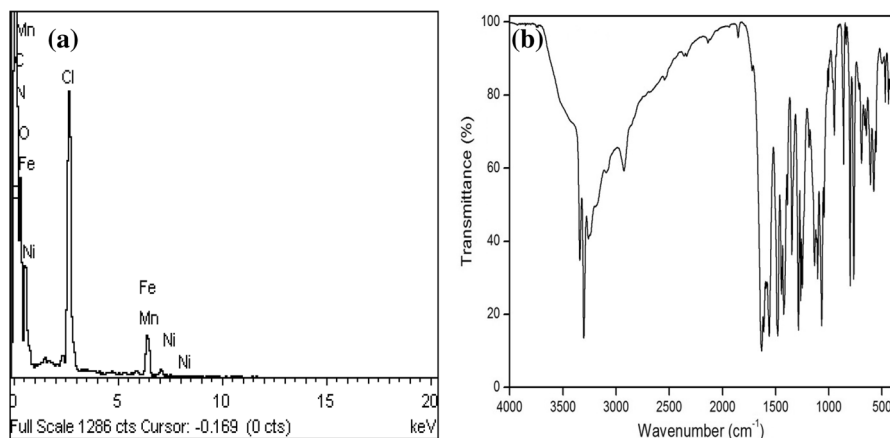


**Fig. 1** EDS (a) and FTIR (b) spectra of  $\text{Ni}_{0.9}\text{Mn}_{0.1}\text{Fe}_2(\text{C}_8\text{H}_5\text{Cl}_2\text{O}_3)\cdot\text{N}_2\text{H}_4$

( $1590\text{ cm}^{-1}$ ) and symmetric ( $1350\text{ cm}^{-1}$ ) stretching frequencies of carboxylate found at  $240\text{ cm}^{-1}$ , which indicates the monodentate linkage [24] of the carboxylate group. The strong peak occurred at  $1250\text{ cm}^{-1}$  indicated the C–O–C stretching frequency. The N–N stretching frequency at  $948\text{ cm}^{-1}$  confirmed the bidentate bridging nature of hydrazine [24]. The C–Cl stretching vibration was observed with the intense peak at  $670\text{ cm}^{-1}$ , respectively. The band at  $462\text{ cm}^{-1}$  proved the metal–oxygen stretching vibration [30].

The thermal decomposition of the precursor occurred in four endothermic mass loss steps (Fig. 2). The initial step is a weak endothermic peak. The mass loss of 7.53% was observed from room temperature to  $160\text{ }^\circ\text{C}$  due to dehydrazination. The strong endotherm was observed in the region  $160\text{--}313\text{ }^\circ\text{C}$  due to the beginning of decarboxylation. In the region  $313\text{--}641\text{ }^\circ\text{C}$ , complete decarboxylation takes place and yields  $\text{Ni}_{0.9}\text{Mn}_{0.1}\text{Fe}_2\text{O}_4$  nanoparticles from the hydrazine precursor. From the analytical, EDS, FTIR and thermal data, the molecular stoichiometric composition [31] of the precursor was assigned as  $\text{Ni}_{0.9}\text{Mn}_{0.1}\text{Fe}_2(\text{C}_8\text{H}_5\text{Cl}_2\text{O}_3)\cdot\text{N}_2\text{H}_4$ .

### Characterization of $\text{Ni}_{0.9}\text{Mn}_{0.1}\text{Fe}_2\text{O}_4$ nanoparticles

The FTIR spectrum of  $\text{Ni}_{0.9}\text{Mn}_{0.1}\text{Fe}_2\text{O}_4$  nanoparticles (Fig. 3a) shows an intense and sharp band in the region  $530\text{ cm}^{-1}$  corresponding to M–O stretching. The other characteristic bands of N–N, N–H, C–O–C, C–Cl, asymmetric and symmetric stretching frequencies observed in the precursor (Fig. 1b) had vanished. Compared to the EDS spectra of the precursor (Fig. 1a) with the nanoparticles (Fig. 3b), the later mainly composed of Ni, Mn, Fe and O and the elements in the precursor N, C, O and Cl were absent. This indicated that hydrazine and carboxylate moieties in the precursor were thermally decomposed. Thus, the formation of  $\text{Ni}_{0.9}\text{Mn}_{0.1}\text{Fe}_2\text{O}_4$  nanoparticles from the precursor was confirmed.

Figure 4a shows the XRD pattern of  $\text{Ni}_{0.9}\text{Mn}_{0.1}\text{Fe}_2\text{O}_4$  nanoparticles. All the diffraction peaks (220), (311), (222), (400), (331), (422), (511), (440), (442), (533),

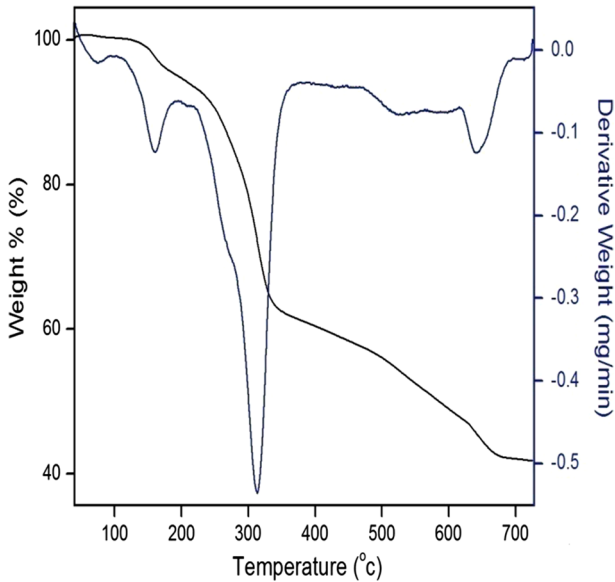


**Fig. 2** TG-DTA curve of Ni<sub>0.9</sub>Mn<sub>0.1</sub>Fe<sub>2</sub>(C<sub>8</sub>H<sub>5</sub>Cl<sub>2</sub>O<sub>3</sub>)·N<sub>2</sub>H<sub>4</sub>

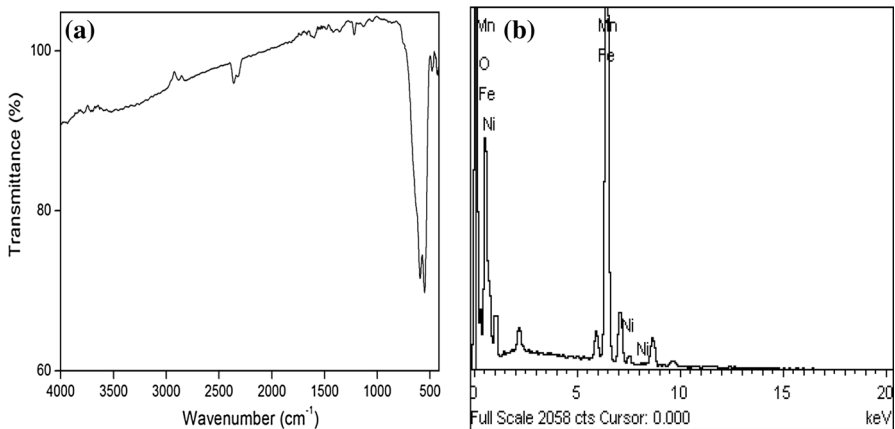


**Fig. 3** FTIR spectrum (a) and EDS image (b) of Ni<sub>0.9</sub>Mn<sub>0.1</sub>Fe<sub>2</sub>O<sub>4</sub> nanoparticles

(622), (444), (711) and (642) in XRD pattern are in good agreement with the JCPDS card nos 74-2081 (NiFe<sub>2</sub>O<sub>4</sub>), 73-1964 (MnFe<sub>2</sub>O<sub>4</sub>). The sharp and intense peaks in XRD revealed their nanocrystalline nature [32]. The SAED pattern (Fig. 4b) shows several bright spots due to the agglomeration within the particles. From Scherrer's formula, the average grain size of the nanoparticles was calculated as 28 nm.

Figure 5a shows a SEM image of Ni<sub>0.9</sub>Mn<sub>0.1</sub>Fe<sub>2</sub>O<sub>4</sub> nanoparticles. As seen in the image, the particles exhibit agglomerated morphology due to magnetic interaction

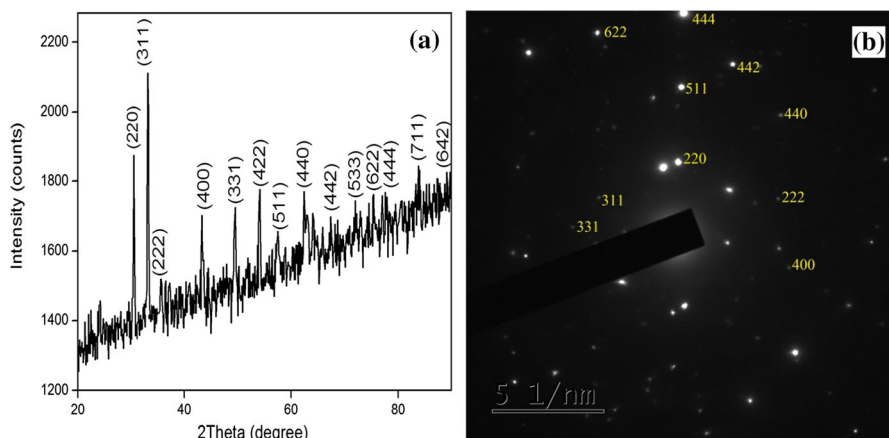


**Fig. 4** XRD spectrum (a) and SAED pattern (b) of  $\text{Ni}_{0.9}\text{Mn}_{0.1}\text{Fe}_2\text{O}_4$  nanoparticles

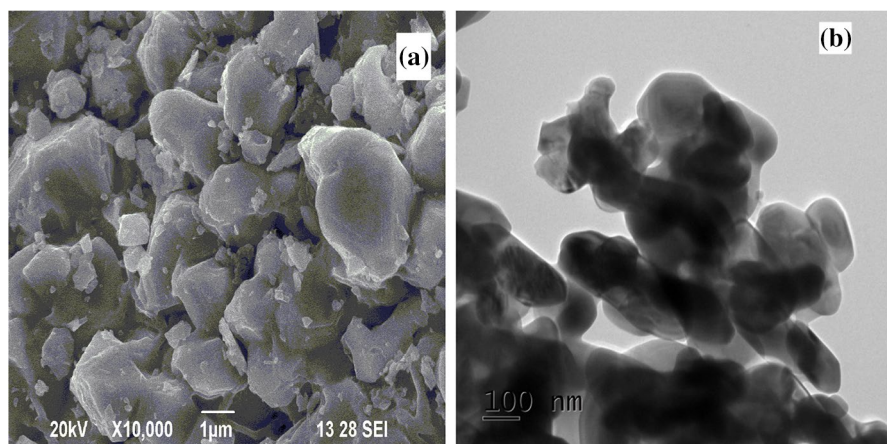


**Fig. 5** SEM image (a) and TEM image (b) of  $\text{Ni}_{0.9}\text{Mn}_{0.1}\text{Fe}_2\text{O}_4$  nanoparticles

between the particles. Figure 5b presents a TEM image of the nanoparticles which were interconnected with each other. The particle size observed from TEM is around 30 nm, which was matched closely with the size calculated by Scherrer's equation.

Figure 6a illustrates the room-temperature magnetic parameter measurement of  $\text{Ni}_{0.9}\text{Mn}_{0.1}\text{Fe}_2\text{O}_4$  nanoparticles. From the results, the saturation magnetization ( $M_s$ -0.1737 emu  $\text{g}^{-1}$ ), remanent magnetization ( $M_r$ -49.568 emu  $\text{g}^{-1}$ ) and coercivity ( $H_c$ -236.48 Oe) of the nanoparticles were observed. The hysteresis loop revealed the soft magnetic nature and excellent magnetic property of the nanoparticle. Therefore, the nanoparticles can be separated from an aqueous solution using an external magnet as seen in the inset of Fig. 6a. UV-DRS of  $\text{Ni}_{0.9}\text{Mn}_{0.1}\text{Fe}_2\text{O}_4$  nanoparticles (Fig. 6b) exhibits strong absorption between 200 and 800 nm and the absorption edge at 430 nm. The optical band gap ( $E_g$ ) can be calculated as 2.88 eV.

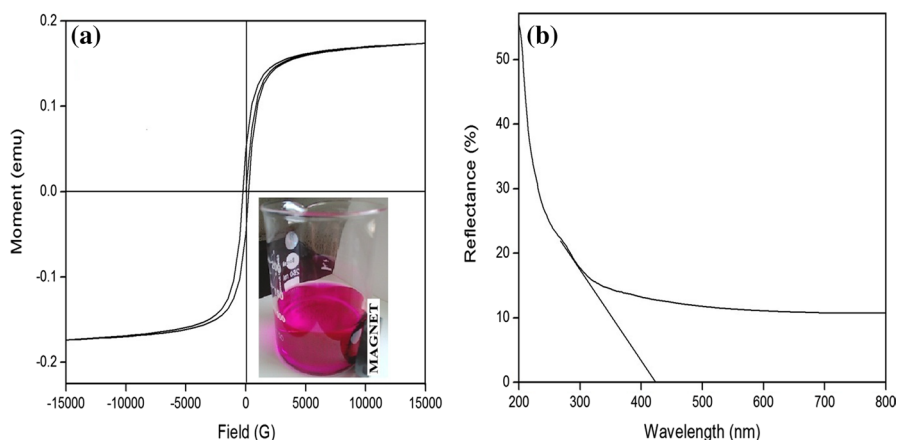


**Fig. 6** VSM hysteresis loop of Ni<sub>0.9</sub>Mn<sub>0.1</sub>Fe<sub>2</sub>O<sub>4</sub> nanoparticles, the inset shows the magnetic separation using an external magnet (a) UV-DRS spectrum of Ni<sub>0.9</sub>Mn<sub>0.1</sub>Fe<sub>2</sub>O<sub>4</sub> nanoparticles (b)

### Photocatalytic property and adsorption kinetics

The photocatalytic activity of Ni<sub>0.9</sub>Mn<sub>0.1</sub>Fe<sub>2</sub>O<sub>4</sub> nanoparticles on anionic and cationic dyes with different reaction time: RhB (60 min), CR and MB (50 min), MG and RB (40 min) and MR (30 min) under bright sunlight, was evaluated. In the mean time, the blank reaction was also evaluated. The photocatalytic degradation of the dyes was shown to follow the order: RB > RhB > MB > MG > CR > MR (Fig. 7a). And there was no change in the degradation of dyes without the photocatalyst. Thus, it can be clearly seen that all the dyes degraded efficiently using Ni<sub>0.9</sub>Mn<sub>0.1</sub>Fe<sub>2</sub>O<sub>4</sub> as a photocatalyst under sunlight. The degradation efficiency percentages of RB, RhB, MB, MG, CR and MR were 98%, 86%, 85%, 83%, 65% and 62%, respectively. The catalyst showed an excellent photocatalytic activity on all the dyes. The degradation of dyes occurred only in the presence of catalyst and sunlight.

Figure 7b reveals the relationship between the time and the equilibrium adsorption ( $q_e$ ) of different dyes on Ni<sub>0.9</sub>Mn<sub>0.1</sub>Fe<sub>2</sub>O<sub>4</sub> photocatalyst. Equation (1) is used to calculate the equilibrium uptake.

$$q_e = \frac{(C_0 - C_e)V}{W} \quad (1)$$

where  $q_e$  is the amount of dye adsorbed by catalyst at equilibrium,  $C_0$  is the initial concentration of the dye solution in mg L<sup>-1</sup>,  $C_e$  is the equilibrium concentration of the dye solution in mg L<sup>-1</sup>,  $V$  is the volume of the solution in mL and  $W$  is the mass of catalyst in milligram taken for the experiments. It is obvious that there was a great adsorption of RB, RhB and MB, while there was a moderate adsorption of MG, CR and MR. The adsorption of RB was the highest among other dyes. However, the Ni<sub>0.9</sub>Mn<sub>0.1</sub>Fe<sub>2</sub>O<sub>4</sub> photocatalyst showed good adsorption capacity on cationic dyes than anionic dyes.

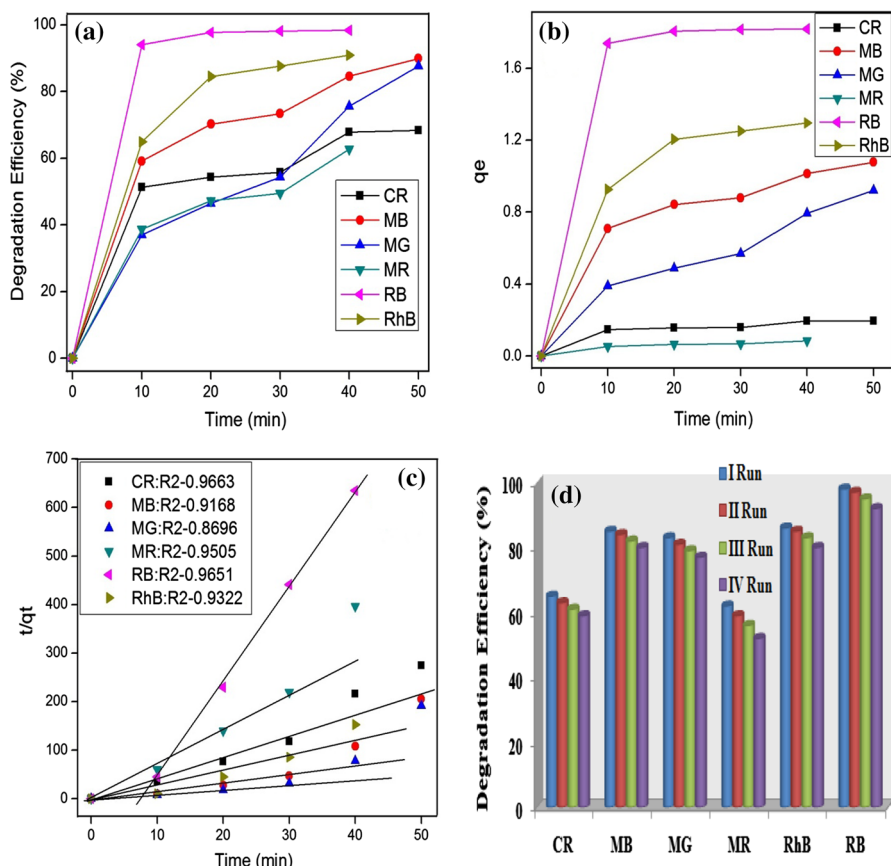


**Fig. 7** Photocatalytic degradation efficiency: (a) adsorption capacity, (b) pseudo-second-order kinetic plots, (c) recycling ability (d) of  $\text{Ni}_{0.9}\text{Mn}_{0.1}\text{Fe}_2\text{O}_4$  photocatalyst

According to the linear plot of  $t/q_t$  versus  $t$  (Fig. 7c) the correlation coefficient  $R^2$  concluded that the pseudo-second-order adsorption model was suitable for fitting the adsorption kinetics. Equation (2) represents the adsorption kinetics which is explained by second-order model.

$$\frac{t}{q_t} = \frac{1}{k_2 q_e^2} + \frac{t}{q_e} \quad (2)$$

where  $k_2$  is the rate constant for second-order adsorption ( $\text{g mg}^{-1}\text{min}^{-1}$ ) and  $q_e$  and  $k_2$  were determined from slope and intercept of plot  $t/q_t$  versus  $t$  (Fig. 7c) for various dyes. The kinetic rate constants ( $K_2$ ) of  $\text{Ni}_{0.9}\text{Mn}_{0.1}\text{Fe}_2\text{O}_4$  nanoparticles on CR (4.0621  $\text{g/mg/min}$ ), MB (1.7817  $\text{g/mg/min}$ ), MG (1.0193  $\text{g/mg/min}$ ), MR (7.9619  $\text{g/mg/min}$ ), RhB (3.5166  $\text{g/mg/min}$ ) and RB (18.4636  $\text{g/mg/min}$ ) were calculated. Thus, the nanoparticle was highly active on anionic dyes especially on RB.



When compared to our previous research work [11], it is visible that the degradation efficiency percentage of Ni<sub>0.9</sub>Mn<sub>0.1</sub>Fe<sub>2</sub>O<sub>4</sub> photocatalyst was relatively high. The major reason for this difference is due to the substitution of different metals in the ferrite system. Moreover, the degradation capacity of Ni<sub>0.9</sub>Mn<sub>0.1</sub>Fe<sub>2</sub>O<sub>4</sub> photocatalyst may be altered by the nature and structure of organic (cationic/anionic) dyes, especially the position of substituent in the aromatic rings present in it.

Due to the highest efficiency and good magnetic property shown by the Ni<sub>0.9</sub>Mn<sub>0.1</sub>Fe<sub>2</sub>O<sub>4</sub> photocatalyst, the endurance has also been examined on all dyes by the recycling process. In this process, the catalyst was separated from the aqueous solution by an external magnet as shown in the inset of Fig. 6a and recycled for further runs under sunlight irradiation. The photocatalyst has analyzed for four runs, and it showed superb endurance with promising photocatalytic ability (Fig. 7d). On the fourth run, the photocatalyst showed the lowest photodegradation on MR than the other dyes. However, the photodegradation efficiency percentage of Ni<sub>0.9</sub>Mn<sub>0.1</sub>Fe<sub>2</sub>O<sub>4</sub> photocatalyst was decreased on all dyes after each cycle.

## Conclusion

The hydrazine precursor Ni<sub>0.9</sub>Mn<sub>0.1</sub>Fe<sub>2</sub>(C<sub>8</sub>H<sub>5</sub>Cl<sub>2</sub>O<sub>3</sub>)·N<sub>2</sub>H<sub>4</sub> was prepared via a coprecipitation technique, successfully. From the analytical and mass loss percentages, the chemical formula of the precursor was fixed. The formation of Ni<sub>0.9</sub>Mn<sub>0.1</sub>Fe<sub>2</sub>O<sub>4</sub> nanoparticle from the precursor by decomposition method was confirmed from thermal, IR, XRD and EDS analyses. The agglomerated Ni<sub>0.9</sub>Mn<sub>0.1</sub>Fe<sub>2</sub>O<sub>4</sub> nanoparticle indicated the grain size as 28 nm. Moreover, the soft magnetic nanoparticle showed the energy band gap as 2.88 eV. The magnetic Ni<sub>0.9</sub>Mn<sub>0.1</sub>Fe<sub>2</sub>O<sub>4</sub> photocatalyst exhibits amazing degradation efficiency on all dyes under direct sunlight. Due to an excellent magnetic property shown by the catalyst, it can be magnetically separated and recycled.

**Acknowledgements** The authors are thankful to Kongunadu Arts and Science College, Coimbatore, for providing facilities. We acknowledge the provision of the necessary facilities by SAIF Cochin, IIT Madras, and Karunya Institute of Technology and Sciences, Coimbatore. One of the authors acknowledge Sri Ramakrishna Engineering College, Coimbatore.

## Compliance with ethical standards

**Conflict of interest** The authors declare that they have no conflict of interest.

## References

1. M. Balakrishnan, S.A. Antony, S. Gunasekaran, R.K. Natarajan, *Indian J. Sci. Technol.* **1**, 1 (2008)
2. H. Wang, T. Wang, B. Zhang, F. Li, B. Toure, I.B. Omosa, *Clean Soil Air Water* **42**, 1029 (2014)
3. Z. Carmen, S. Daniela, in *Organic Pollutants Ten Years After the Stockholm Convention-Environmental and Analytical Update*, ed. By T. Puzyn (In Tech, 2012), p. 55
4. R. Kant, *Nat. Sci.* **4**, 22 (2012)
5. H. Zhou, D.W. Smith, *J. Environ. Eng. Sci.* **1**, 247 (2002)

6. X. Qu, P.J.J. Alvarez, Q. Li, *Water Res.* **47**, 3931 (2013)
7. A. Ahmad, S.H.M. Setapar, S.C. Chuo, A. Khattoon, W.A. Wani, R. Kumar, *RSC Adv.* **5**, 30801 (2015)
8. M.I. Litter, *Appl. Catal. B Environ.* **23**, 89 (1999)
9. E. Casbeer, V.K. Sharma, X.-Z. Li, *Sep. Purif. Technol.* **87**, 1 (2012)
10. N. Masunga, O.K. Mmelesi, K.K. Kefeni, B.B. Mamba, *J. Environ. Chem. Eng.* **7**, 3 (2019)
11. O. Raina, R. Manimekalai, *Res. Chem. Int.* **44**, 5941 (2018)
12. C. Barathiraja, A. Manikandan, A.M.U. Mohideen, S. Jayasree, S.A. Antony, *J. Supercond. Nov. Magn.* **29**, 477 (2016)
13. G. Mathubala, A. Manikandan, S.A. Antony, P. Ramar, *J. Mol. Struct.* **1113**, 79 (2016)
14. L.G.V. Uitert, *J. Chem. Phys.* **23**, 306 (1956)
15. S. Gubbala, H. Nathani, K. Koizol, R.D.K. Misra, *Phys. B* **348**, 317 (2004)
16. E.R. Kumar, A.S. Kamzin, T. Prakash, *J. Magn. Magn. Mater.* **378**, 389 (2015)
17. Z. Zhang, Q. Tan, Z. Zhong, F. Su, *RSC Adv.* **5**, 40018 (2015)
18. B.V. Tirupanyam, C. Srinivas, S.S. Meena, S.M. Yusuf, A.S. Kumar, D.L. Sastry, *J. Magn. Magn. Mater.* **392**, 101 (2015)
19. M. Khan, J. Duan, Y. Chen, H. Yao, S. Lyu, H. Shou, *J. Alloys Compd.* **701**, 147 (2017)
20. M.K. Zate, S.M.F. Shaikh, V.V. Jadhav, K.K. Tehare, S.S. Kolekar, R.S. Mane, *J. Anal. Appl. Pyrolysis* **116**, 177 (2015)
21. E.R. Kumar, P.S.P. Reddy, G.S. Devi, S. Sathiyaraj, *J. Magn. Magn. Mater.* **398**, 281 (2016)
22. T.F. Marinca, I. Chicinaş, O. Isnard, B.V. Neamţu, *Ceram. Int.* **42**, 4754 (2016)
23. R.S. Pandav, R.P. Patil, S.S. Chavan, I.S. Mulla, P.P. Hankare, *J. Magn. Magn. Mater.* **417**, 407 (2016)
24. A. Braibanti, F. Dallavalle, M.A. Pellinghelli, E. Leporati, *Inorg. Chem.* **7**, 1430 (1968)
25. T. Premkumar, S. Govindarajan, A.E. Coles, C.A. Wight, *J. Phys. Chem. B* **109**, 6126 (2005)
26. K. Thangavelu, K. Parameswari, K. Kuppusamy, Y. Haldorai, *Mater. Lett.* **65**, 1482 (2011)
27. S.G. Gawas, V.M.S. Verenkar, *Thermochim. Acta* **605**, 16 (2015)
28. P.P.G. Desai, V.M.S. Verenkar, *J. Mater. Sci. Mater. Electron.* **29**, 6924 (2018)
29. A.I. Vogel, *Vogel's Text book of Quantitative Chemical Analysis*, 5th edn. (Longmann, London, 1989), p. 384
30. M.G. Naseri, E.B. Saion, M. Hashim, A.H. Shaari, H.A. Ahangar, *Solid State Commun.* **151**, 1031 (2011)
31. U.B. Gawas, V.M.S. Verenkar, *Thermochim. Acta* **556**, 41 (2013)
32. R.C.C. Monteiro, A.A.S. Lopes, M.M.R.A. Lima, J.P.B. Veiga, *J. Non-Cryst. Solids* **491**, 124 (2018)

**Publisher's Note** Springer Nature remains neutral with regard to jurisdictional claims in published maps and institutional affiliations.